Geophysical Research Letters

RESEARCH LETTER
10.1029/2023GL105642

# On the Vertical Structure of Mesoscale Eddies in the Kuroshio-Oyashio Extension

**H. Yao[1,2], C. Ma[1,2], Z. Jing[1,2], and Z. Zhang[1,2]**

[1]Frontier Science Center for Deep Ocean Multispheres and Earth System and Physical Oceanography Laboratory, Ocean University of China, Qingdao, China, [2]Laoshan Laboratory, Qingdao, China

**Key Points:**

- Three vertical structures of mesoscale eddies are classified in the Kuroshio-Oyashio Extension region
- Mesoscale eddy splitting or merging causes significant variation of vertical eddy structures
- Different vertical eddy structures can be partially accounted for by baroclinic instabilities and local adjustment process

**Supporting Information:**

Supporting Information may be found in the online version of this article.

**Correspondence to:**

C. Ma,
machao@ouc.edu.cn

**Citation:**

Yao, H., Ma, C., Jing, Z., & Zhang, Z. (2023). On the vertical structure of mesoscale eddies in the Kuroshio-Oyashio extension. *Geophysical Research Letters*, *50*, e2023GL105642. https://doi.org/10.1029/2023GL105642

Received 26 JUL 2023
Accepted 30 NOV 2023



**Abstract** Vertical structure of mesoscale eddies is key to the eddy-induced heat/material transport that further affects the climate and marine ecosystem. This study explores the vertical structure of mesoscale eddies in the Kuroshio-Oyashio Extension region (KOE) and its underlying dynamics. By applying the hierarchical ascending classification to the observational and reanalysis data sets, we classify mesoscale eddies with three distinct kinds of vertical structures. Each kind of eddies exhibits clear spatial aggregation along a distinct zonal band. Eddies have core depths of 100–300 m in the northern part of the KOE and core depths of 300–500 m and 0–100 m in the southern. The eddy splitting or merging does not introduce new kind of eddy vertical structure but causes large intra-kind variability. The different kinds of eddy vertical structures can be partially accounted for by the baroclinic instabilities at the eddy generation sites and local adjustment process.

**Plain Language Summary** Mesoscale eddies are swirling motions with a radius ranging from several tens to a hundred of kilometers. The mesoscale eddies can cause strong vertical displacement of isopycnals, yet the vertical structure of such displacement has not been well understood. This study examines the vertical structures of mesoscale eddies in the Kuroshio-Oyashio Extension region based on the observational and reanalysis data sets. Mesoscale eddies with three distinct kinds of vertical structures are identified. Both the eddy generation and local adjustment during eddy propagation play important roles in the vertical structures of eddies.

## 1. Introduction

Mesoscale eddies are ubiquitous in the upper ocean. Although the surface signals of mesoscale eddies have been well depicted based on satellite measurements, their vertical structures are less understood but play a critical role in the eddy-induced heat/material transports. These transports have been shown to exert significant influences on the large-scale ocean thermal structure (Yu et al., 2019), anthropogenic climate changes (Du et al., 2022), ocean's biogeochemical cycles (McGillicuddy et al., 1998, 2007), dispersion of marine pollutants (Gilchrist et al., 2020) and microplastics behavior (Cai et al., 2022).

The Kuroshio-Oyashio Extension (KOE) region, located near the western boundary of North Pacific, consists of several prominent fronts including the subarctic front (SAF), the subarctic boundary, the Kuroshio bifurcation front and the Kuroshio extension (KE) (Figure 1). The KOE region is characterized as a zone with elevated eddy kinetic energy (EKE) (Qiu & Chen, 2010; Figure 1) and also a hotspot for mid-latitude air-sea heat and carbon dioxide exchanges (Fassbender et al., 2017; Jing et al., 2020). A knowledge of the vertical structure of mesoscale eddies within the KOE region is thus essential for understanding the eddies' climate and ecological impacts. By compositing all the mesoscale eddies around the KE front, Sun et al. (2017) reported that the eddy core measured by density anomaly is on average located around 300–400 m. In contrast, Dong et al. (2017) observed a deeper eddy core in the south of the KE front than the north and attributed this vertical difference to the poleward shoaling of thermocline. Ding and Jing (2020) analyzed the zonal variation of the eddy vertical structure, identifying double-core eddies in the upper stream of the KE front.

Although these previous studies have advanced the understanding of eddy vertical structures in the KOE region, they suffer from several limitations. First, the previous studies dealt with the mean eddy vertical structure in some pre-defined subdomains of the KOE region. It remains elusive from such analysis how many there are distinct kinds of eddy vertical structures in the KOE region. Second, the previous studies analyzed the eddy vertical structure under a Eulerian framework and thus did not take into account the evolution of eddy vertical structure during the eddy life cycle. In particular, it is still unclear whether the eddy vertical structure would change significantly

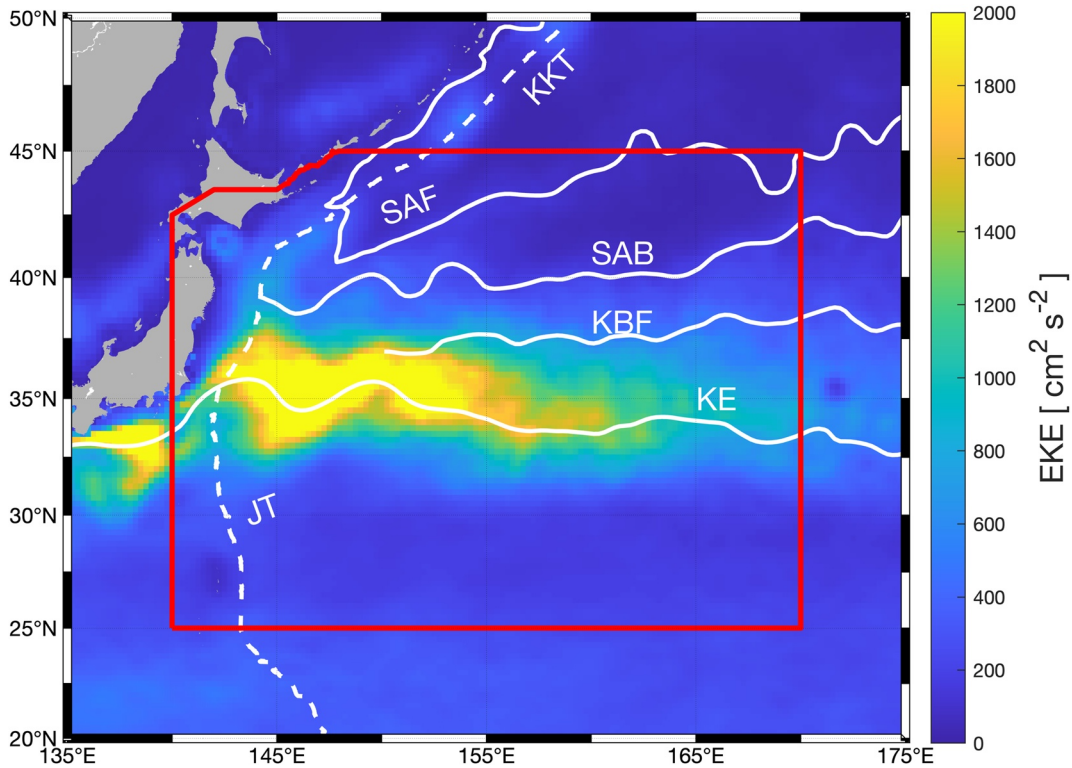


**Figure 1.** Climatological mean eddy kinetic energy (EKE; unit: $cm^2s^{-2}$) from Archiving, Validation and Interpretation of Oceanographic Satellite data (AVISO) (Aviso Altimetry, 2022). The Japan Trench and Kuril-Kamchatka Trench are represented by the dashed white lines. The subarctic front, the subarctic boundary, the Kuroshio bifurcation front and the Kuroshio extension are represented by white thick lines and are recognized by AVISO mean dynamic topography contour following Nakano et al. (2018). The red box is our research region.

during the eddy splitting or merging process. Third, mesoscale eddies in the KOE region are generated primarily from the baroclinic instability especially for those large enough to be well identified from the satellite altimeters (Ji et al., 2018; H. Yang et al., 2018). A natural question is that to what extent the distinct eddy vertical structures in the KOE region can be accounted for by the baroclinic instability.

Recently, clustering techniques have been leveraged to analyze oceanic data (Sambe & Suga, 2022). Surface-intensified and subsurface-intensified eddies have been distinguished via the hierarchical ascending classification (HAC) for the four primary eastern boundary upwelling systems (Pegliasco et al., 2015). In contrast to traditional approaches that manually subdivide areas for analysis, the HAC is capable of offering an impartial classification of mesoscale eddies based on the mathematical similarity of their vertical structures.

In this study, we explore the vertical structure of mesoscale eddies in the KOE region under a Lagrangian framework, by applying the HAC to the observational and reanalysis data sets. The paper is organized as follows. Section 2 details the data and methods. The vertical structures of mesoscale eddies as well as their changes during the eddy splitting or merging are documented in Section 3. Section 4 discusses the role of baroclinic instability of eddy generation and local adjustment process in shaping the eddy vertical structure. The paper is ended with a summary of its major conclusions.

## 2. Data and Methods

### 2.1. Observational Data

Surface mesoscale eddies within the KOE region (135–175°E; 25–45°N) are detected and tracked using daily maps of delayed-time multimission absolute dynamic topography and derived geostrophic velocity fields (UV) (E.U. Copernicus Marine Service Information (CMEMS), 2022). The data span a period of 22 years (from January 2000 to December 2021) and have a spatial resolution of 1/4°. There are 3,056 anticyclonic eddies

(AEs) and 3,787 cyclonic eddies (CEs) detected and tracked in total via the TOEddies algorithm (Laxenaire et al., 2019). Only mesoscale eddies possessing more than five Argo profiles within the maximum eddy velocity boundary during their lifespan are retained for further analysis. After a quality control of the Argo data (see Text S1 in Supporting Information S1), there are 7,214 (4,821) Argo profiles in 476 AEs and 404 CEs used for analysis.

### 2.2. Reanalysis Data

Given the limitations in the spatio-temporal coverage of observational data, we have also utilized the Four-Dimensional Variational Ocean Reanalysis for the Western North Pacific over 30 Years (FORA-WNP30) (Usui et al., 2017) to analyze the vertical structure of mesoscale eddies and their underlying dynamics. The FORA-WNP30 offers a spatial resolution of 1/10° for the majority of the research region, and 1/6° for the remainder. To align with the period during which the assimilated altimeter-derived sea surface height (SSH) was recorded, we only use model output from January 1993 to December 2014. From the FORA-WNP30 data, we detected and tracked 5,100 AEs and 6,371 CEs in total.

### 2.3. The Ocean Eddy Detection and Tracking Algorithms (TOEddies)

The TOEddies algorithm (Laxenaire et al., 2018, 2019), developed from the widely used geometric algorithm (Chaigneau et al., 2008, 2009; Pegliasco et al., 2015), is used to detect and track mesoscale eddies. The TOEddies algorithm does not only provide information on eddy dynamical characteristics such as radius and velocity but also constructs a sophisticated eddy network. This network connects eddy trajectories associated with merging with other eddies or splitting into multiple eddies, enabling the tracking the origin of individual eddies.

Once an eddy is detected, eddy anomalies are calculated by subtracting a local climatological mean profile. For the observational data, local climatological mean profiles of potential temperature $\theta$, salinity $S$ and potential density $\sigma$ are derived from the World Ocean Atlas 2018 (WOA18) 1/4° objectively analyzed monthly climatology following Laxenaire et al. (2020). These fields are linearly interpolated to match the position and day of the year of each Argo float. For the reanalysis data, eddy anomalies are calculated by subtracting a large-scale background field. The large-scale background of some variable, including $\theta$, $S$, $\sigma$ and horizontal velocity ($u$,$v$) is first computed as its climatological mean on each calendar day over a 22-year period. Then this climatological mean field is further smoothed horizontally using a 41 × 41 grid boxcar filter and temporally using a 31-day running mean filter. The EKE is computed as $\mathrm{EKE} = \left(u'^2 + v'^2\right)/2$, where $u'$ and $v'$ are velocity anomaly.

### 2.4. Cluster Analysis

To classify mesoscale eddies with different vertical structures, we implement the HAC technique following Pegliasco et al. (2015) to eddies in the observational and reanalysis data sets. Due to the complexity of mesoscale eddies in the KOE region, the vertical profiles of $\theta'/S'/\sigma'$ at the centroids of the eddies and the average EKE profile along the SSH contour with the maximum eddy velocity are considered for a substantial classification.

All the vertical profiles are first linearly interpolated onto a 10-m regular grid from the surface to 1,000 m, as the eddy signal below 1,000 m in our research region is very weak. Then the vertical profiles of an eddy along its trajectory at different snapshots are averaged to form a single vertical profile. To remove potential obscure clusters classified by the HAC, following Laxenaire et al. (2020) we discard weak eddies that have a maximum value of any vertical profile of $\theta'/S'/\sigma'$ less than 0.1 °C/psu/kg $\mathrm{m}^{-3}$. This criterion is applied to both the eddies in the observational and reanalysis data to keep consistency, yielding 394 (297) AEs (CEs) in the observational data and 3,130 (4,001) AEs (CEs) in the reanalysis data. Note that the much smaller number of eddies in the observation is due to the sparsity of Argo profiles.

The HAC method first treats each eddy's vertical profiles of $\theta'/S'/\sigma'$ (and also EKE for the reanalysis data) as a unique cluster, subsequently merging similar clusters to form a unified cluster that encompasses all the eddies' vertical profiles. The merging process involves the three stages: calculating Euclidean distances of the normalized (dimensionless) vertical profiles between eddies; grouping closest eddies into a dendrogram using Ward's aggregation method (Ward, 1963); and finally selecting an optimal cut point in the cluster tree to partition the eddies into different clusters based on the significant difference in their vertical structures (Text S2; Table S1;

Figure S1 and S2 in Supporting Information S1). Readers can refer to Pegliasco et al. (2015) for more details of the HAC method.

## 3. Results

### 3.1. Vertical Structures of Mesoscale Eddies

Application of the HAC method to the observational data suggests that the vertical structures of AEs and CEs in the KOE region can be classified into three distinct clusters (Figure 2). The first cluster, including 112 (28%) AEs and 117 (39%) CEs, is characterized by strong $\theta'/S'/\sigma'$ between 100 and 300 m (Figures 2a, 2g, 2m, 2s, 2d, 2j, 2p, and 2v). These eddies are predominantly located in the northern part (35°N–45°N) of the KOE region, consistent with the findings reported by Itoh and Yasuda (2010). Tracking analysis reveals that many AEs and CEs in this cluster originate from the SAF, the Kuril-Kamchatka Trench and downstream KE (Figures S3 and S4 in Supporting Information S1). The AEs (CEs) included in this cluster tend to carry positive (negative) $\theta'$ and $S'$ values with the former dominating $\sigma'$. The typical peaking values $\theta'/S'/\sigma'$ in the vertical are 1.97°C, 0.17 psu, and −0.20 kg m$^{-3}$ for AEs and −1.91°C, −0.22 psu, and 0.15 kg m$^{-3}$ for CEs, respectively. The water mass analysis implies that these eddies should carry Okhotsk sea mode water (Gladyshev et al., 2003; Yasuda, 1997) and transition region mode water (Saito et al., 2007), which is consistent with their origins derived from the tracking analysis (Figure S5 in Supporting Information S1).

The second cluster includes 164 (42%) AEs and 138 (46%) CEs, exhibiting strong $\theta'/S'/\sigma'$ between 300 and 500 m (Figures 2b, 2h, 2n, 2t, 2e, 2k, 2q, and 2w). This cluster is distributed around the center and to the south of the KE axis, located within the warm and salty region of the North Pacific Subtropical Mode Water (STMW) (Masuzawa, 1969) and lighter central mode water (Oka et al., 2011) (Figure S5 in Supporting Information S1). Some eddies in this cluster are shed off via the meandering of the KE (Ding & Jing, 2020), while others originate to the south of the KE axis or from the central North Pacific (Figures S3 and S4 in Supporting Information S1). This cluster displays typical peaking values of $\theta'/S'/\sigma'$ as 3.25°C, 0.22 psu, and −0.38 kg m$^{-3}$ for AEs and −2.62°C, −0.22 psu, and 0.33 kg m$^{-3}$ for CEs.

The third cluster comprises 118 (30%) AEs and 42 (14%) CEs. The $\theta'/S'/\sigma'$ of these eddies are near-surface intensified and have relatively smaller amplitudes than those in the first and second clusters (Figures 2c, 2i, 2o, 2u, 2f, 2l, 2r, and 2x). Typical peaking values of $\theta'/S'/\sigma'$ in this cluster are 1.08°C, 0.14 psu, and −0.26 kg m$^{-3}$ for AEs, and −0.75°C, −0.10 psu, and 0.33 kg m$^{-3}$ for CEs. This cluster of eddies is located in the southernmost part of the KOE region and partially overlapped with the second cluster of eddies in space. These eddies tend to form locally or originate from the central North Pacific, carrying warm and salty STMW (Figures S3 to S5 in Supporting Information S1). To the best of our knowledge, this third eddy cluster has not been documented in the existing literature. Due to the spatial overlap of the second and third clusters, and the weaker amplitude of the third cluster, it is difficult to identify the third cluster based on the eddy composite analysis over a pre-defined region as done in the previous studies (Dong et al., 2017; Ji et al., 2018; Sun et al., 2017).

Finally, it is found that the three distinct eddy clusters in the observations are consistently reproduced in the reanalysis data (Figure S6 in Supporting Information S1) and in a smaller domain (29°N–45°N) excluding eddies from the subtropical countercurrent (Figure S7 in Supporting Information S1). The statistical analysis of surface characteristics within each cluster reveals notable distinctions among them (Table S2 and S3 in Supporting Information S1). Moreover, whether including the vertical profile of EKE in the HAC method does not qualitatively affect the identified eddy clusters in the reanalysis data (Figures S6 and S8 in Supporting Information S1). In the following analysis, we will focus on the eddy clusters in the reanalysis data as its sample number of eddies is much larger than that in the observation, yielding a more robust statistic.

### 3.2. Influences of Eddy Merging and Splitting on Vertical Structures of Mesoscale Eddies

In the KOE region, displacement and deformation of mesoscale eddies cause frequent eddy merging and splitting. Among the total 5,100 (6,371) AEs (CEs) detected in the reanalysis data, only 2,226 (2,326) always evolve as a single coherent vortex. The remainings merge with other eddies or split into multiple eddies sometime during their life cycles. In specific, there are 1,624 (2,168) AEs (CEs) undergoing merging events and 1,250 (1,877) undergoing splitting events.

To examine the effects of eddy merging and splitting on the eddy vertical structures, we compute the vertical displacement of peaking depth of $\sigma'$ during the merging and splitting events (denoted as $d_m$ and $d_s$). Here the vertical displacement is estimated as the difference between the peaking depths of $\sigma'$ 15 days before and after merging

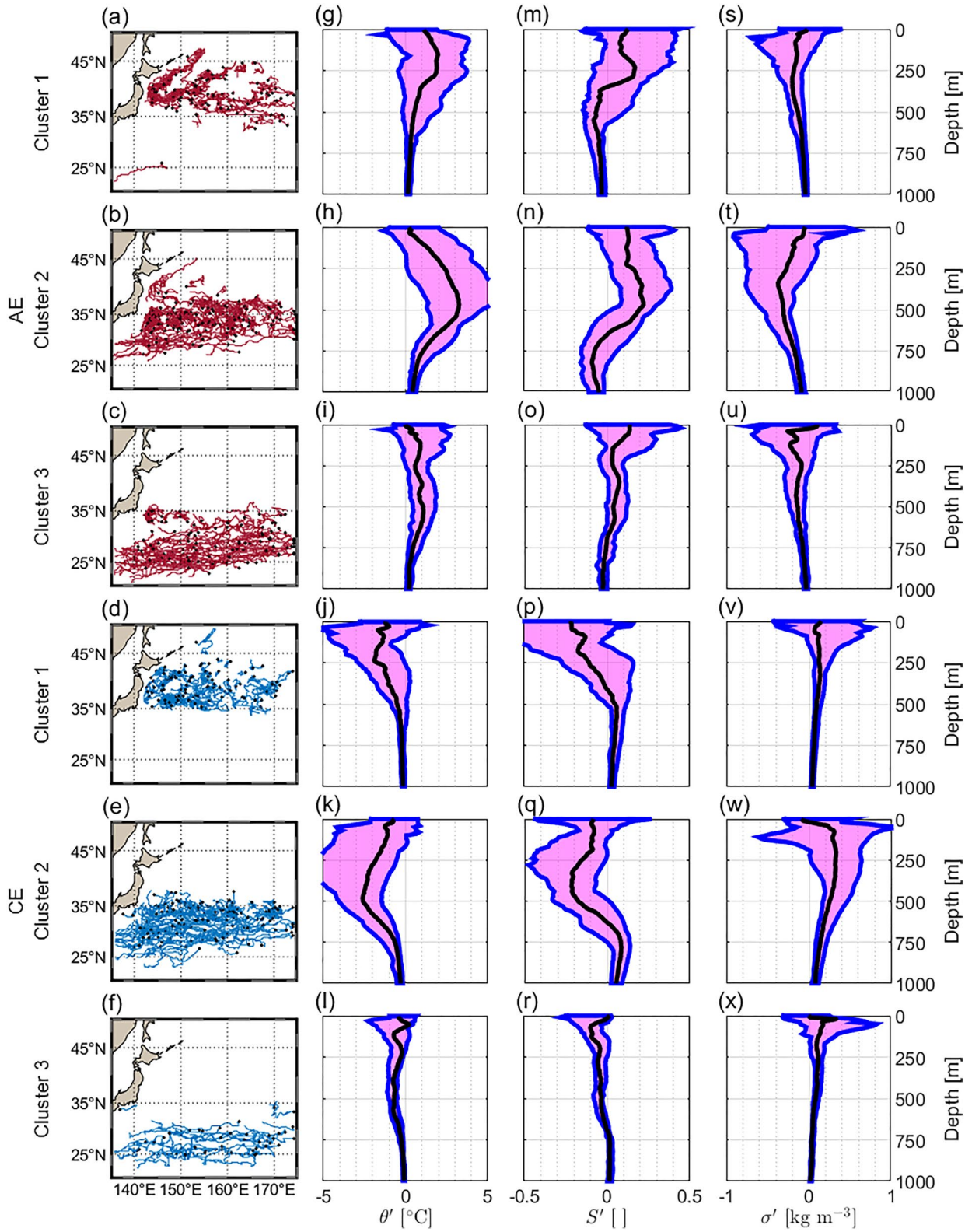


**Figure 2.** Spatial distributions and vertical structures ($\theta'/S'/\sigma'$) of eddies for each cluster in the observational data. (a–f) The trajectories of eddies (red/blue line indicate anticyclonic eddies/cyclonic eddies, the black diamond markers show the birth location), vertical profiles of (g–l) potential temperature, (m–r) salinity and (s–x) potential density anomaly for each eddy clusters. The black curve in each functional boxplot (Genton & Sun, 2020; Sun & Genton, 2011) is the median vertical profile and the magenta box is the 50% central region.

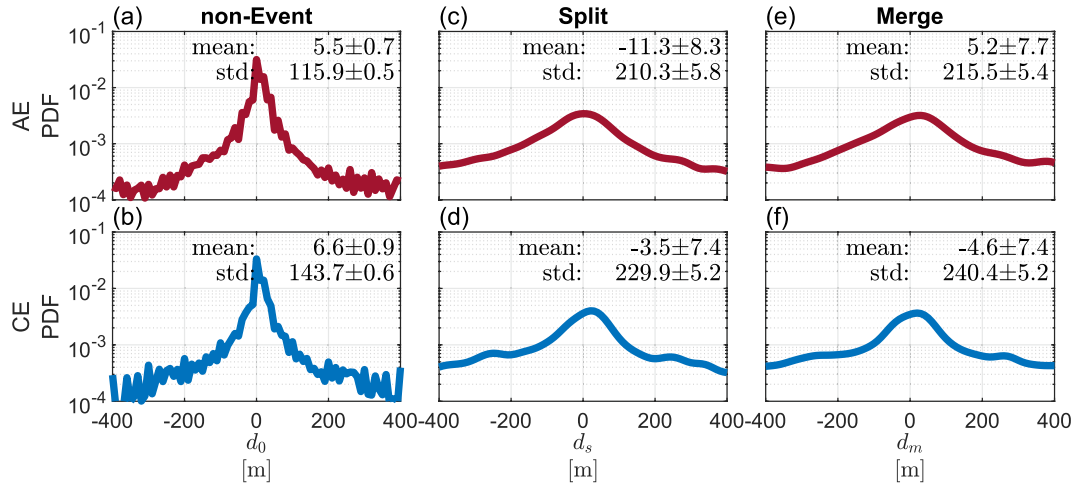


**Figure 3.** Probability density function of vertical displacement of peaking depth of $\sigma'$ during the eddy merging, splitting events and otherwise (non-event). The errorbar denotes the 95% confidence intervals of the mean and standard deviation of vertical displacement.

and splitting events. Sensitivity tests suggest that varying the time span from 10 to 20 days or using the peaking depth of $\theta'$ and $S'$ do not have substantial impacts on the results (Figure S9 in Supporting Information S1). It should be noted that the peaking depth of $\sigma'$ during a 30-day-long period is likely to change even without the occurrence of eddy merging and splitting events. Therefore, the values of $d_m$ and $d_s$ should be compared to that when eddy merging and splitting do not occur (denoted as $d_0$).

Figure 3 presents the probability density functions of $d_m$, $d_s$ and $d_0$. The mean value and standard deviation of $d_0$ are 5.5 ± 0.7 (6.6 ± 0.9) m and 115.9 ± 0.5 (143.7 ± 0.6) m for AEs (CEs), respectively (the errorbars denote the 95% confidence intervals, and hereinafter). The standard deviation of $d_m$ for AEs (CEs) increases to 215.5 ± 5.4 (240.4 ± 5.2) m, significantly larger than that of $d_0$. Similar is the case for $d_s$, suggesting that the eddy merging and splitting have notable effects on the eddy vertical structures. Unlike the standard deviation, the difference among mean values of $d_m$, $d_s$ and $d_0$ are minor. It thus suggests that the eddy merging and splitting should be unlikely to introduce new clusters of eddy vertical structures but instead enlarge the intra-cluster variability. This is further confirmed by applying the HAC method to eddies experiencing merging/splitting during the life cycles or not, respectively. The resultant eddy vertical structures of three clusters are consistent with those derived from all the eddies (Figures S10 and S11 in Supporting Information S1).

## 4. Discussion

To shed light on the underlying dynamics on the three different clusters of vertical structures of mesoscale eddies in the KOE region, we perform a linear baroclinic instability (LBI) analysis at generation sites and a vertical mode analysis at the positions during eddy movements. The LBI analysis is based on the inviscid quasi-geostrophic potential vorticity (QGPV) equation (Feng et al., 2022).

$$q_t + \boldsymbol{U}\cdot\nabla q + \boldsymbol{u}\cdot\nabla Q = 0, \quad -H < z < 0 \tag{1}$$

$$\varphi_{zt} + \boldsymbol{U}\cdot\nabla\varphi_z + \boldsymbol{u}\cdot\nabla\left(\varphi_z + f^{-1}N^2\eta\right) = 0, \quad z = 0, -H, \tag{2}$$

where $\boldsymbol{U} = U(z)\vec{i} + V(z)\vec{j}$ is the mean current, $Q = \beta y + \vec{k}\cdot\nabla\times\boldsymbol{U} - g/\rho_0\partial_z\left(f\rho/N^2\right)$ is the mean potential vorticity with $\beta$ the local planetary vorticity gradient, $N^2$ the background squared buoyancy frequency, $\rho_0$ the reference density and $f$ the Coriolis parameter, $q = \nabla^2\varphi + \Gamma\varphi$ is the eddy component of the QGPV with $\Gamma = \partial_z(f^2/N^2\partial_z)$ the vortex stretching operator, $\boldsymbol{u} = -\varphi_y\vec{i} + \varphi_x\vec{j}$ is the eddy velocity field expressed in terms of the horizontal eddy stream function $\varphi = \varphi(x, y, z, t)$, $\nabla\varphi_z = V_z\vec{i} - U_z\vec{j}$ is proportional to the mean horizontal buoyancy gradient via the thermal wind relation, $\eta$ is the bottom topography height at $z = -H$ and $\eta = 0$ at $z = 0$, and $\nabla = \vec{i}\frac{\partial}{\partial x} + \vec{j}\frac{\partial}{\partial y}$ is the horizontal gradient operator.

Contrary to the previous LBI analysis performed over fixed regions (e.g., Jing et al., 2019), we apply the LBI analysis to individual eddies. In specific, the LBI analysis is computed based on the background field at the generation

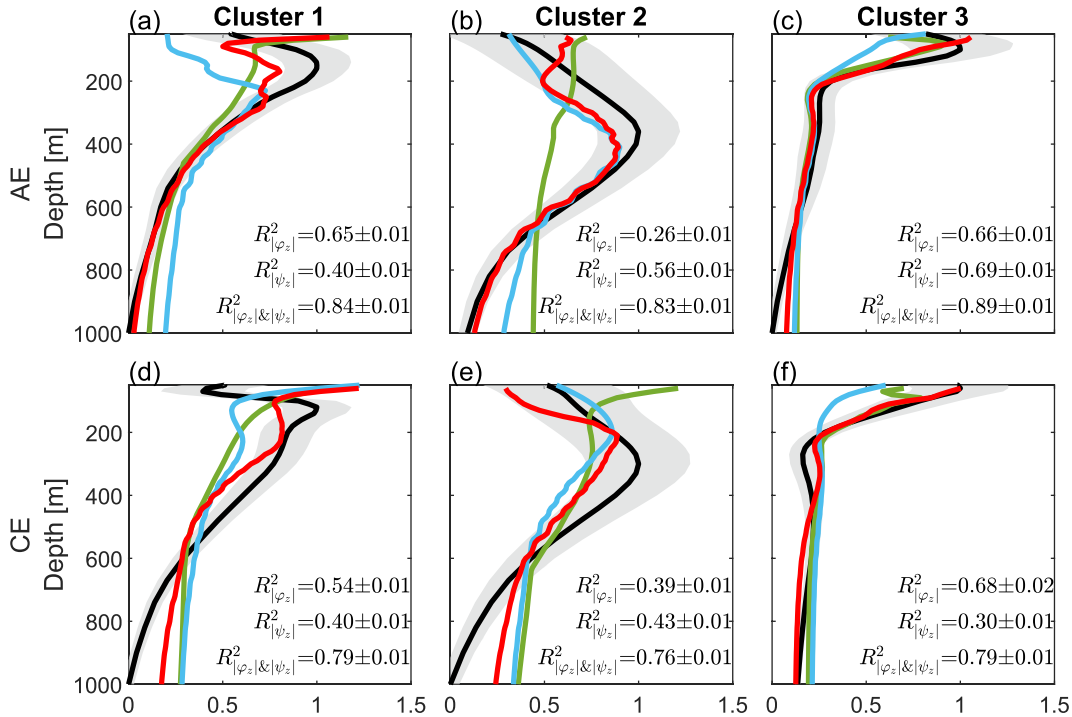


**Figure 4.** Vertical profiles of normalized $\sigma'$ (black) and its prediction from linear regression to normalized $|\varphi_z|$ (green), normalized $|\psi_z|$ (blue) and their combination (red) for anticyclonic eddies (a–c) and cyclonic eddies (d–f) of different clusters. Each profile corresponds to the median profile in the functional boxplots, and the gray shading is the standard deviation of $\sigma'$. The numbers in each panel show the median $R^2$ and its confidence interval.

sites of individual eddies. To exclude the mixed-layer baroclinic instability (MLI) generating eddies at submesoscales, the upper boundary is moved from the sea surface to the 50-m depth. The detailed procedures for searching fastest-growing baroclinic instability (BCI) mode at mesoscales can be found in Feng et al. (2021, 2022).

There are, however, several limitations for the LBI analysis. First, it can only account for mesoscale eddies generated primarily via the baroclinic instabilities. Second, it does not take into consideration the adjustment of eddy vertical structure to the local stratification (Pedlosky, 1987). In the observation, stream functions of eddies are found to be dominated by the first baroclinic mode $\psi(z)$ derived from the Sturm-Liouville eigenvalue problem (Gill, 1982) and barotropic mode (Zhang et al., 2013), suggesting the important role of local adjustment to stratification and planetary rotation in shaping the eddy vertical structure. To evaluate the effects of baroclinic instability at eddy generation site and local adjustment during eddy propagation, we first normalize $\sigma'$ of each eddy so that it ranges from 0 to 1 vertically, regress the normalized $\sigma'$ to the normalized $|\varphi_z|$ and $|\psi_z|$, use the variance explained by the regression model $R^2$ as a measurement.

When both $|\varphi_z|$ and $|\psi_z|$ are chosen as predictors of the regression model, the predicted $\sigma'$ agrees qualitatively with the true value and captures the distinct vertical structures of the three eddy clusters (Figure 4). The median $R^2$ over the eddies of different polarization and clusters ranges from 0.76 to 0.89, significantly higher than that for the regression to $|\varphi_z|$ or $|\psi_z|$ alone. It thus suggests that both the baroclinic instability at eddy generation sites and local adjustment process play an important role in shaping the vertical structure of eddies and can partially account for the different vertical structures of three eddy clusters.

## 5. Conclusions

In this study, we utilize a clustering technique to classify the typical vertical structures of mesoscale eddies in the KOE region based on the observational and reanalysis data. According to the vertical profiles of $\theta'/S'/\sigma'$, three distinct eddy clusters are identified. The first cluster has core depths of 100–300 m and is located in the northern part of the KOE. The second and third clusters has core depths of 300–500 m and 0–100 m, respectively. These two clusters are located in the southern part of the KOE and overlapped in space. The eddy splitting or merging

causes strong variability of vertical structures of $\theta'/S'/\sigma'$, enlarging their intra-cluster variability. Dynamical analysis suggest that the three clusters of eddy vertical structures can be partially accounted for by the baroclinic instabilities and local adjustment process. Further research is needed to better comprehend the underlying dynamics governing the eddy vertical structures, including the effects of barotropic instability, eddy-mean flow, and eddy-eddy interactions.

The cluster analysis uncovers a new type of eddy vertical structure in the south of KOE region, which is overlooked in the existing literature (Dong et al., 2017; Jing et al., 2019; W. Sun et al., 2017). On the one hand, this discovery expands our comprehension of the vertical structure of mesoscale eddies within the KOE region. On the other hand, it highlights the usefulness of statistical learning like cluster analysis in oceanography research. We remark that previous studies (Chaigneau et al., 2011; Dong et al., 2017; Keppler et al., 2018) computed the mean eddy vertical structure in some pre-defined subdomains based on the subjective premise that eddies in each subdomain should have a unique vertical structure. This premise, however, is invalid in the south of KOE region and mix up two different kinds of eddy vertical structures there. The cluster analysis gets rids of this premise and provides a more reliable classification of eddy vertical structures. Combination of dynamical analysis and advanced statistical learning could improve our understanding of eddy origins, characteristics as well as their induced heat and material transports that are crucial to the climate and marine ecological system (Chang et al., 2020; Chelton et al., 2011).

## Data Availability Statement

The altimeter products are available in E.U. Copernicus Marine Service Information (CMEMS) (2022). The Argo data are available in Argo Data Management Team (2022). The climatological data WOA18 (World Ocean Atlas 2018) are available in Boyer et al. (2018), Locarnini et al. (2019a, 2019b) and Zweng et al. (2019). The reanalysis data FORA-WNP30 (Four-dimensional Variational Ocean ReAnalysis for the Western North Pacific) are available in Usui and Usui et al. (2017). The radius of deformation data are available in Chelton et al. (1998). The seasonal mean EKE data are available in SSALTO/DUACS (2022).

**Acknowledgments**
This research was supported by the National Natural Science Foundation of China (No.41676004). We thank Dr. Laxenaire for providing the TOEddies algorithm code and application testing.

## References

Argo Data Management Team. (2022). Argo user's manual (3.41.1) [Dataset]. https://doi.org/10.13155/29825

Aviso Altimetry. (2022). SSALTO/DUACS user handbook: Climatologies products [Dataset]. Retrieved from https://www.aviso.altimetry.fr/en/data/products/sea-surface-height-products/global/gridded-sea-level-anomalies-mean-and-climatology.html

Boyer, T. P., Garcia, H. E., Locarnini, R. A., Zweng, M. M., Mishonov, A. V., Reagan, J. R., et al. (2018). World Ocean Atlas 2018 [dataset]. NOAA National Centers for Environmental Information. Retrieved from https://www.ncei.noaa.gov/archive/accession/NCEI-WOA18

Cai, M., Liu, M., Qi, H., Cui, Y., Zhang, M., Huang, P., et al. (2022). Transport of microplastics in the South China Sea: A review. *Gondwana Research*, *108*, 49–59. https://doi.org/10.1016/j.gr.2021.12.003

Chaigneau, A., Eldin, G., & Dewitte, B. (2009). Eddy activity in the four major upwelling systems from satellite altimetry (1992–2007). *Progress in Oceanography*, *83*(1–4), 117–123. https://doi.org/10.1016/j.pocean.2009.07.012

Chaigneau, A., Gizolme, A., & Grados, C. (2008). Mesoscale eddies off Peru in altimeter records: Identification algorithms and eddy spatio-temporal patterns. *Progress in Oceanography*, *79*(2–4), 106–119. https://doi.org/10.1016/j.pocean.2008.10.013

Chaigneau, A., Le Texier, M., Eldin, G., Grados, C., & Pizarro, O. (2011). Vertical structure of mesoscale eddies in the eastern South Pacific Ocean: A composite analysis from altimetry and Argo profiling floats. *Journal of Geophysical Research*, *116*(C11). https://doi.org/10.1029/2011JC007134

Chang, P., Zhang, S., Danabasoglu, G., Yeager, S. G., Fu, H., Wang, H., et al. (2020). An unprecedented set of high-resolution earth system simulations for understanding multiscale interactions in climate variability and change. *Journal of Advances in Modeling Earth Systems*, *12*(12), e2020MS002298. https://doi.org/10.1029/2020MS002298

Chelton, D. B., de Szoeke, R. A., & Michael, G. S. (1998). Global Atlas of the first-baroclinic Rossby radius of deformation and gravity-wave phase speed [dataset]. https://ceoas.oregonstate.edu/rossby_radius

Chelton, D. B., Gaube, P., Schlax, M. G., Early, J. J., & Samelson, R. M. (2011). The influence of nonlinear mesoscale eddies on near-surface oceanic chlorophyll. *Science*, *334*(6054), 328–332. https://doi.org/10.1126/science.1208897

Ding, Y., & Jing, C. (2020). Three-dimensional thermohaline anomaly structures of rings in the Kuroshio Extension region. *Acta Oceanologica Sinica*, *39*(3), 25–35. https://doi.org/10.1007/s13131-020-1559-3

Dong, D., Brandt, P., Chang, P., Schütte, F., Yang, X., Yan, J., & Zeng, J. (2017). Mesoscale eddies in the northwestern Pacific Ocean: Three-dimensional eddy structures and heat/salt transports. *Journal of Geophysical Research: Oceans*, *122*(12), 9795–9813. https://doi.org/10.1002/2017JC013303

Du, T., Jing, Z., Wu, L., Wang, H., Chen, Z., Ma, X., et al. (2022). Growth of ocean thermal energy conversion resources under greenhouse warming regulated by oceanic eddies. *Nature Communications*, *13*(1), 7249. https://doi.org/10.1038/s41467-022-34835-z

E.U. Copernicus Marine Service Information (CMEMS). (2022). Global Ocean gridded L 4 sea surface heights and derived variables reprocessed 1993 ongoing [Dataset]. https://doi.org/10.48670/moi-00148

Fassbender, A. J., Sabine, C. L., Cronin, M. F., & Sutton, A. J. (2017). Mixed-layer carbon cycling at the Kuroshio extension observatory. *Global Biogeochemical Cycles*, *31*(2), 272–288. https://doi.org/10.1002/2016GB005547

Feng, L., Liu, C., Köhl, A., Stammer, D., & Wang, F. (2021). Four types of baroclinic instability waves in the global oceans and the implications for the vertical structure of mesoscale eddies. *Journal of Geophysical Research: Oceans*, *126*(3). https://doi.org/10.1029/2020JC016966

Feng, L., Liu, C., Köhl, A., & Wang, F. (2022). Seasonality of four types of baroclinic instability in the global oceans. *Journal of Geophysical Research: Oceans*, *127*(5). https://doi.org/10.1029/2022JC018572

Genton, M. G., & Sun, Y. (2020). Functional data visualization. In N. Balakrishnan, T. Colton, B. Everitt, W. Piegorsch, F. Ruggeri, & J. L. Teugels (Eds.), *Wiley StatsRef: Statistics reference online* (1st ed., pp. 1–11). Wiley. https://doi.org/10.1002/9781118445112.stat08290

Gilchrist, R. M., Hall, R. A., Bacon, J. C., Rees, J. M., & Graham, J. A. (2020). Increased dispersion of oil from a deep water seabed release by energetic mesoscale eddies. *Marine Pollution Bulletin*, *156*, 111258. https://doi.org/10.1016/j.marpolbul.2020.111258

Gill, A. (1982). *Atmosphere-ocean dynamics* (1st ed.). Academic Press. Retrieved from https://shop.elsevier.com/books/atmosphere-ocean-dynamics/gill/978-0-12-283522-3

Gladyshev, S., Talley, L., Kantakov, G., Khen, G., & Wakatsuchi, M. (2003). Distribution, formation, and seasonal variability of Okhotsk Sea Mode water. *Journal of Geophysical Research*, *108*(C6). https://doi.org/10.1029/2001JC000877

Itoh, S., & Yasuda, I. (2010). Characteristics of mesoscale eddies in the Kuroshio–Oyashio extension region detected from the distribution of the sea surface height anomaly. *Journal of Physical Oceanography*, *40*(5), 1018–1034. https://doi.org/10.1175/2009JPO4265.1

Ji, J., Dong, C., Zhang, B., Liu, Y., Zou, B., King, G. P., et al. (2018). Oceanic eddy characteristics and generation mechanisms in the Kuroshio Extension region. *Journal of Geophysical Research: Oceans*, *123*(11), 8548–8567. https://doi.org/10.1029/2018JC014196

Jing, Z., Chang, P., Shan, X., Wang, S., Wu, L., & Kurian, J. (2019). Mesoscale SST dynamics in the Kuroshio–Oyashio Extension region. *Journal of Physical Oceanography*, *49*(5), 1339–1352. https://doi.org/10.1175/JPO-D-18-0159.1

Jing, Z., Wang, S., Wu, L., Chang, P., Zhang, Q., Sun, B., et al. (2020). Maintenance of mid-latitude oceanic fronts by mesoscale eddies. *Science Advances*, *6*(31), eaba7880. https://doi.org/10.1126/sciadv.aba7880

Keppler, L., Cravatte, S., Chaigneau, A., Pegliasco, C., Gourdeau, L., & Singh, A. (2018). Observed characteristics and vertical structure of mesoscale eddies in the southwest tropical Pacific. *Journal of Geophysical Research: Oceans*, *123*(4), 2731–2756. https://doi.org/10.1002/2017JC013712

Laxenaire, R., Speich, S., Blanke, B., Chaigneau, A., Pegliasco, C., & Stegner, A. (2018). Anticyclonic eddies connecting the western boundaries of Indian and Atlantic Oceans. *Journal of Geophysical Research: Oceans*, *123*(11), 7651–7677. https://doi.org/10.1029/2018JC014270

Laxenaire, R., Speich, S., & Stegner, A. (2019). Evolution of the thermohaline structure of one Agulhas ring reconstructed from satellite altimetry and Argo floats. *Journal of Geophysical Research: Oceans*, *124*(12), 8969–9003. https://doi.org/10.1029/2018JC014426

Laxenaire, R., Speich, S., & Stegner, A. (2020). Agulhas ring heat content and transport in the south Atlantic estimated by combining satellite altimetry and Argo profiling floats data. *Journal of Geophysical Research: Oceans*, *125*(9). https://doi.org/10.1029/2019JC015511

Locarnini, R. A., Boyer, T. P., Mishonov, A. V., Reagan, J. R., Zweng, M. M., Baranova, O. K., et al. (2019a). World Ocean Atlas 2018 [dataset]. In A. Mishonov (Ed.), (Technical Ed.), *Density* (Vol. 5). NOAA Atlas NESDIS 85. Retrieved from https://www.ncei.noaa.gov/archive/accession/NCEI-WOA18

Locarnini, R. A., Mishonov, A. V., Baranova, O. K., Boyer, T. P., Zweng, M., García, H. E., et al. (2019b). World ocean atlas 2018 [dataset]. In A. Mishonov (Ed.), (Technical Ed.), *Temperature* (Vol. 1). NOAA Atlas NESDIS 81. Retrieved from https://www.ncei.noaa.gov/archive/accession/NCEI-WOA18

Masuzawa, J. (1969). Subtropical mode water. *Deep Sea Research and Oceanographic Abstracts*, *16*(5), 463–472. https://doi.org/10.1016/0011-7471(69)90034-5

McGillicuddy, D. J., Anderson, L. A., Bates, N. R., Bibby, T., Buesseler, K. O., Carlson, C. A., et al. (2007). Eddy/wind interactions stimulate extraordinary mid-ocean Plankton Blooms. *Science*, *316*(5827), 1021–1026. https://doi.org/10.1126/science.1136256

McGillicuddy, D. J., Robinson, A. R., Siegel, D. A., Jannasch, H. W., Johnson, R., Dickey, T. D., et al. (1998). Influence of mesoscale eddies on new production in the Sargasso Sea. *Nature*, *394*(6690), 263–266. https://doi.org/10.1038/28367

Nakano, H., Tsujino, H., Sakamoto, K., Urakawa, S., Toyoda, T., & Yamanaka, G. (2018). Identification of the fronts from the Kuroshio Extension to the Subarctic Current using absolute dynamic topographies in satellite altimetry products. *Journal of Oceanography*, *74*(4), 393–420. https://doi.org/10.1007/s10872-018-0470-4

Oka, E., Kouketsu, S., Toyama, K., Uehara, K., Kobayashi, T., Hosoda, S., & Suga, T. (2011). Formation and subduction of central mode water based on profiling float data, 2003–08. *Journal of Physical Oceanography*, *41*(1), 113–129. https://doi.org/10.1175/2010JPO4419.1

Pedlosky, J. (1987). *Geophysical fluid dynamics*. Springer. Retrieved from http://link.springer.com/10.1007/978-1-4612-4650-3

Pegliasco, C., Chaigneau, A., & Morrow, R. (2015). Main eddy vertical structures observed in the four major Eastern Boundary Upwelling Systems. *Journal of Geophysical Research: Oceans*, *120*(9), 6008–6033. https://doi.org/10.1002/2015JC010950

Qiu, B., & Chen, S. (2010). Eddy-mean flow interaction in the decadally modulating Kuroshio Extension system. *Deep Sea Research Part II: Topical Studies in Oceanography*, *57*(13–14), 1098–1110. https://doi.org/10.1016/j.dsr2.2008.11.036

Saito, H., Suga, T., Hanawa, K., & Watanabe, T. (2007). New type of pycnostad in the western subtropical-subarctic transition region of the North Pacific: Transition region mode water. *Journal of Oceanography*, *63*(4), 589–600. https://doi.org/10.1007/s10872-007-0052-3

Sambe, F., & Suga, T. (2022). Unsupervised clustering of Argo temperature and salinity profiles in the mid-latitude Northwest Pacific ocean and revealed influence of the Kuroshio extension variability on the vertical structure distribution. *Journal of Geophysical Research: Oceans*, *127*(3), e2021JC018138. https://doi.org/10.1029/2021JC018138

SSALTO/DUACS. (2022). Monthly mean and climatology maps of sea level anomalies [dataset]. https://www.aviso.altimetry.fr/en/data/products/sea-surface-height-products/global/gridded-sea-level-anomalies-mean-and-climatology.html

Sun, W., Dong, C., Wang, R., Liu, Y., & Yu, K. (2017). Vertical structure anomalies of oceanic eddies in the Kuroshio Extension region. *Journal of Geophysical Research: Oceans*, *122*(2), 1476–1496. https://doi.org/10.1002/2016JC012226

Sun, Y., & Genton, M. G. (2011). Functional boxplots. *Journal of Computational & Graphical Statistics*, *20*(2), 316–334. https://doi.org/10.1198/jcgs.2011.09224

Usui, N. (2017). Four-dimensional Variational Ocean ReAnalysis for the Western North Pacific (FORA-WNP30) [Dataset]. Retrieved from https://www.godac.jamstec.go.jp/fora/e/index.html

Usui, N., Wakamatsu, T., Tanaka, Y., Hirose, N., Toyoda, T., Nishikawa, S., et al. (2017). Four-dimensional variational ocean reanalysis: A 30-year high-resolution dataset in the Western North Pacific (FORA-WNP30). *Journal of Oceanography*, *73*(2), 205–233. https://doi.org/10.1007/s10872-016-0398-5

Ward, J. H. (1963). Hierarchical grouping to optimize an objective function. *Journal of the American Statistical Association*, *58*(301), 236–244. https://doi.org/10.1080/01621459.1963.10500845

Yang, G., Wang, F., Li, Y., & Lin, P. (2013). Mesoscale eddies in the northwestern subtropical Pacific Ocean: Statistical characteristics and three-dimensional structures. *Journal of Geophysical Research: Oceans*, *118*(4), 1906–1925. https://doi.org/10.1002/jgrc.20164

Yang, H., Qiu, B., Chang, P., Wu, L., Wang, S., Chen, Z., & Yang, Y. (2018). Decadal variability of eddy characteristics and energetics in the Kuroshio extension: Unstable versus stable states. *Journal of Geophysical Research: Oceans*, *123*(9), 6653–6669. https://doi.org/10.1029/2018JC014081

Yasuda, I. (1997). The origin of the North Pacific intermediate water. *Journal of Geophysical Research*, *102*(C1), 893–909. https://doi.org/10.1029/96JC02938

Yu, X., Naveira Garabato, A. C., Martin, A. P., Buckingham, C. E., Brannigan, L., & Su, Z. (2019). An annual cycle of submesoscale vertical flow and restratification in the upper ocean. *Journal of Physical Oceanography*, *49*(6), 1439–1461. https://doi.org/10.1175/JPO-D-18-0253.1

Zhang, Z., Zhang, Y., Wang, W., & Huang, R. X. (2013). Universal structure of mesoscale eddies in the ocean. *Geophysical Research Letters*, *40*(14), 3677–3681. https://doi.org/10.1002/grl.50736

Zweng, M. M., Reagan, J. R., Seidov, D., Boyer, T. P., Locarnini, R. A., Garcia, H. E., et al. (2019). World ocean atlas 2018 [dataset]. In A. Mishonov (Ed.), (Technical Ed.), *Salinity* (Vol. 2). NOAA Atlas NESDIS 82. Retrieved from https://www.ncei.noaa.gov/archive/accession/NCEI-WOA18